

Bonding Hierarchy and Coordination Interaction Leading to High Thermoelectricity in Wide Bandgap TlAgI₂

Xiaoying Wang,¹ Mengyang Li,² Minxuan Feng,¹ Xuejie Li,¹ Yuzhou Hao,¹ Wen Shi,^{3,4} Jiangang He,⁵ Xiangdong Ding,¹ and Zhibin Gao^{1,†}

¹State Key Laboratory for Mechanical Behavior of Materials, School of Materials Science and Engineering, Xi'an Jiaotong University, Xi'an 710049, China

²School of Physics, Xidian University, Xi'an 710071, China

³School of Chemistry, Sun Yat-sen University, Guangzhou, Guangdong, 510006, China

⁴Institute of Green Chemistry and Molecular Engineering, Sun Yat-sen University, Guangzhou, Guangdong, 510006, China

⁵School of Mathematics and Physics, University of Science and Technology Beijing, Beijing 100083, China

(Dated: September 6, 2024)

High thermoelectric properties are associated with the phonon-glass electron-crystal paradigm. Conventional wisdom suggests that the optimal bandgap of semiconductor to achieve the largest power factor should be between 6 and $10\kappa_B T$. To address challenges related to the bipolar effect and temperature limitations, we present findings on Zintl-type TlAgI₂, which demonstrates an exceptionally low lattice thermal conductivity of $0.3 \text{ W m}^{-1} \text{ K}^{-1}$ at 300 K. The achieved figure of merit (ZT) for TlAgI₂, featuring a 1.55 eV bandgap, reaches a value of 2.20 for p-type semiconductor. This remarkable ZT is attributed to the existence of extended antibonding states [Ag-I] in the valence band. Furthermore, the bonding hierarchy, influencing phonon anharmonicity, and coordination bonds, facilitating electron transfer between the ligand and the central metal ion, significantly contribute to electronic transport. This finding serves as a promising avenue for the development of high ZT materials with wide bandgaps at elevated temperatures.

I. INTRODUCTION

Thermoelectric technology, offering clean and sustainable means, can directly and reversibly convert heat into electrical energy. Typically, the thermoelectric conversion efficiency is gauged by the dimensionless figure of merit, $ZT = S^2 \sigma T / \kappa$, where S , σ , κ , and T represent the Seebeck coefficient, electrical conductivity, thermal conductivity, and working temperature, respectively. However, these parameters are tightly interconnected, and improving ZT necessitates optimizing the adversely interdependent S , σ , and κ as a collective. Therefore, there are several degrees of freedom to enhance ZT , such as spin, orbital, charge, and lattice [1, 2].

In a given working temperature range, the optimal ZT is constrained by the intrinsic electronic bandgap. Many celebrated narrow bandgap thermoelectric materials, such as PbTe ($E_g=0.28 \text{ eV}$) [3, 4] and (Bi,Sb)₂Te₃ ($E_g=0.13 \text{ eV}$) [5], have been identified. However, the thermoelectric properties are significantly affected when there is a substantial number of both electrons and holes contributing to charge transport, known as bipolar charge transport. This phenomenon occurs when electrons are excited across the bandgap, producing minority charge carriers (e.g., holes in an n-type material) in addition to majority charge carriers (e.g., electrons in an n-type material). Bipolar effects are observed in small bandgap materials at high temperatures ($k_B \sim E_g$). Consequently, the Seebeck coefficient is dramatically affected because the minority charge carriers add a Seebeck voltage of the opposite sign to the majority carriers,

greatly reducing the thermopower $|S|$ [6–11]. Moreover, narrow-gap semiconductors cannot be effectively utilized at higher temperatures.

By employing a good rule of thumb, $E_g = 2eS_{max}T$ [12], where S_{max} is the maximum Seebeck coefficient, and e is the unit charge, wide bandgap semiconductors could mitigate the bipolar effect and temperature range limitations [13–15]. In other words, wide bandgap semiconductors have the potential to overcome the restrictions of narrow bandgap materials and serve as promising thermoelectric candidates. For example, the three-element Heusler Li₂NaSb, with a 1.72 eV bandgap, achieves a ZT value of 1.20 [16]. A copper-tin compound, Cu₂Se, with a 1.20 eV bandgap, exhibits a ZT value of 1.40 [17]. The stannide tin compounds Cu₂ZnSnSe₄, featuring a 1.44 eV bandgap, demonstrate a ZT value of 0.75 [18, 19]. However, all these systems have ZT values below 2.0, primarily due to poor electrical properties and high lattice thermal conductivity (κ_L).

In this study, we leverage chemical bonding hierarchy and coordination interaction to enhance the transport properties of the wide bandgap material TlAgI₂. The concept of chemical bond hierarchy involves ionic bonding, covalent bonding, and coordination interaction [20–22], which explains the coexistence of weak and rigid bonds within materials. In materials undergoing thermally induced large amplitude vibrations, such as La₂Zr₂O₇ [23] and Bi₄O₄SeCl₂ [24], the intrinsic coexistence of rigid crystalline sublattices and fluctuating non-crystalline sublattices is observed. This atomic-level heterogeneity results in vibrational modes that generate a

mismatch in the phonon density of states, thereby enhancing phonon anharmonicity and reducing κ_L [25].

We discovered that Zintl-type TlAgI₂ exhibits an ultralow κ_L of 0.30 W m⁻¹ K⁻¹ at 300 K, achieved by considering quartic anharmonicity renormalization and the off-diagonal term of the heat flux operators. Additionally, the weakening of bonds and strong phonon-phonon interactions are attributed to the antibonding states just below the Fermi level in the electronic band structure, arising from interactions between silver 4*d* and iodine 5*p* orbitals. Moreover, the unexpectedly strong hole transport performance, characterized by a large hole density of states, is influenced by the coordination interactions forming a stable coordination complex, Ag-I [26]. The wide bandgap, coupled with high energy band asymmetry, counteracts bipolar effects, resulting in a notably high Seebeck coefficient up to 704 μ V K⁻¹ at a hole concentration of 10¹⁸ at 1200 K. Ultimately, the achieved *ZT* values for TlAgI₂ with a 1.55 eV bandgap reach 2.20 and 1.82 for p-type and n-type concentrations, respectively. This finding suggests the potential of using bonding hierarchy and coordination interactions in designing high-temperature thermoelectric materials with wide bandgaps.

II. COMPUTATIONAL METHODS

Generally, κ_L is the summation of the Peierls contribution from diagonal term κ_p and the Wigner distribution from off-diagonal term κ_c [27], $\kappa_{Total} = \kappa_c + \kappa_p$. Wherein the κ_c originates from Wigner distribution associated with the wave-like tunnelling [27, 28] and loss of coherence between different vibrational eigenstates. The κ_c can be expressed as,

$$\begin{aligned} \kappa_c = & \frac{\hbar^2}{k_B T^2 V N_0} \sum_{\mathbf{q}} \sum_{s \neq s'} \frac{\omega_{\mathbf{q}}^s + \omega_{\mathbf{q}}^{s'}}{2} \mathbf{v}_{\mathbf{q}}^{s,s'} \cdot \mathbf{v}_{\mathbf{q}}^{s',s} \\ & \times \frac{\omega_{\mathbf{q}}^s n_{\mathbf{q}}^s (n_{\mathbf{q}}^s + 1) + \omega_{\mathbf{q}}^{s'} n_{\mathbf{q}}^{s'} (n_{\mathbf{q}}^{s'} + 1)}{4(\omega_{\mathbf{q}}^{s'} - \omega_{\mathbf{q}}^s)^2 + (\Gamma_{\mathbf{q}}^s + \Gamma_{\mathbf{q}}^{s'})^2} \\ & \times (\Gamma_{\mathbf{q}}^s + \Gamma_{\mathbf{q}}^{s'}), \end{aligned} \quad (1)$$

where \hbar , k_B , T , V , N_0 are the reduced Planck constant, Boltzmann constant, absolute temperature, primitive cell volume, and the total number of sampled phonon wave vectors in the first Brillouin zone, respectively. For the Peierls-Boltzmann transport equation, the diagonal contribution κ_p can be calculated as,

$$\kappa_p = \frac{\hbar^2}{k_B T^2 V N_0} \sum_{\lambda} n_{\lambda} (n_{\lambda} + 1) \omega_{\lambda}^2 \mathbf{v}_{\lambda} \otimes \mathbf{v}_{\lambda} \tau_{\lambda}, \quad (2)$$

where κ_p represents the $\kappa_p^{3,4ph}$ considering anharmonic phonon renormalization (APRN) at finite temperatures, three-phonon (3ph) and four-phonon (4ph) scatterings.

It is derived from Peierls contribution related to the particle-like propagation of phonon wave packets. n_{λ} , ω_{λ} , v_{λ} , and τ_{λ} are the equilibrium component of the phonon population, frequency, group velocity, and lifetime for the λ mode (wave vector q and branch index s), respectively. Except for τ_{λ} , all the above parameters can be obtained from harmonic approximation (HA). We adapted 3ph and 4ph scattering from the self-consistent phonon (SCPH) [29] theory to obtain τ_{λ} including anharmonic effects beyond perturbation theory that considers the quantum effect of phonons [30–32].

Among various existing approaches such as self-consistent ab initio lattice dynamics (SCALD) [33] and stochastic self-consistent harmonic approximation (SSCHA) [34], self-consistent phonon (SCPH) approximation is one effective method that can rigorously account for the first-order correction of phonon frequencies from the quartic anharmonicity. The SCPH approach can better describe the soft phonon modes and strong anharmonicity. In brief, the SCPH can be written as [35, 36]

$$\Omega_{\lambda}^2 = \omega_{\lambda}^2 + 2\Omega_{\lambda} \sum_{\lambda_1} I_{\lambda\lambda_1}, \quad (3)$$

where ω_{λ} is the original phonon frequency from the harmonic approximation and Ω_{λ} is the temperature-dependent renormalized phonon frequency. The scalar $I_{\lambda\lambda_1}$ can be obtained by,

$$I_{\lambda\lambda_1} = \frac{\hbar}{8N_0} \frac{V^{(4)}(\lambda, -\lambda, \lambda_1, -\lambda_1)}{\Omega_{\lambda}\Omega_{\lambda_1}} [1 + 2n_{\lambda}(\Omega_{\lambda_1})], \quad (4)$$

in which $V^{(4)}$ is the fourth-order IFCs in the reciprocal representation and phonon population n_{λ} satisfies Bose-Einstein distribution as a function of temperature. Both Eq. (3) and Eq. (4) have parameters $I_{\lambda\lambda_1}$ and Ω_{λ} in common, and thus SCPH equation can be solved iteratively. Note that $I_{\lambda\lambda_1}$ can be interpreted as the interactions between a pair of phonon modes, λ , and λ_1 including the temperature effects [35, 36].

DFT calculations were performed using the *Vienna ab initio simulation package* (VASP) [37] with the projector-augmented wave (PAW) method [38, 39]. We used the PBEsol functional to obtain lattice constants. Cutoff energy of 400 eV was used with $11 \times 11 \times 11$ Monkhorst-Pack k -grids. The self-consistent iteration for the energy convergence criterion was 10⁻⁸ eV, and all geometries were optimized by the conjugate-gradient method until none of the residual Hellmann-Feynman forces exceeded 10⁻⁶ eV/Å. The optimized conventional cell lattice constant of tetragonal I4/mcm phase (No. 140), a=b=8.188 Å, c=7.562 Å. A $2 \times 2 \times 2$ supercell and $5 \times 5 \times 5$ k -points were employed in all finite displacement calculations.

We generated force-displacement data by performing *ab initio* molecular dynamics (AIMD) simulation with a $2 \times 2 \times 2$ supercell at 300 K for 2000 steps with a time

step of 2 fs using a Nosé-Hoover thermostat and 10^{-6} eV energy threshold. We sampled 40 atomic configurations that were equally spaced in time by removing the first 400 steps from the trajectories and then randomly displaced all of the atoms within the supercell by 0.02 Å (second-order) and 0.1 Å (higher-order) in random directions in each configuration to decrease cross-correlations in the sensing matrix formed by products of atomic displacements. Finally, the 40 uncorrelated sets were computed using accurate DFT calculations with a 10^{-8} eV energy convergence threshold. We used $12 \times 12 \times 12$ ngrids for κ_p^{3ph} , and $7 \times 7 \times 7$ for $\kappa_p^{3,4ph}$ and κ_c . The electronic band structure and crystal orbital Hamilton population (COHP) were calculated using a $9 \times 9 \times 9$ k -meshes. The elastic constants, dielectric constants, deformation potential, and wave functions were gained with $12 \times 12 \times 12$ k -meshes. The carrier transport properties were obtained in uniform $41 \times 41 \times 45$ k -point grids in electronic transport [40].

We systematically studied the effect of quartic anharmonicity on the lattice dynamics, electronic transport, and thermal transport properties of TlAgI₂ by leveraging recent advances including (i) compressive sensing lattice dynamics (CSLD) [41–43] to establish the high-order inter-atomic force constants (IFCs), that utilized the compressive sensing technique [44] to select the physically relevant IFCs from the force-displacement data under the constraints enforced by the space group symmetry. (ii) rigorous calculations of temperature-dependent phonons used SCPH theory and higher-order multiphonon scattering rates [35, 45], (iii) evaluation of κ_L employed a unified theory that accounts simultaneously for diagonal term from the standard Peierls contribution and off-diagonal terms from the coherent Wigner distribution [27, 46]. (iv) The Seebeck coefficient, conductivity, and power factor were calculated by considering the electron-phonon coupling such as the acoustic deformation potential, ionized impurity, and polar optical phonon scattering, as implemented in the amset package [40].

III. RESULTS AND DISCUSSION

TlAgI₂ adopts a tetragonal structure (space group I4/mcm [140]), where Tl, Ag, and I occupy the 4a, 4b, and 8h sites with a total of 8 atoms in the primitive cell. In this structure, Tl and I form an octahedral cage [47], illustrated in Fig. 1(a), with the Ag element embedded within the cage. All outcomes take into account the Self-Consistent Phonon (SCPH) effect, except for the Harmonic Approximation (HA). The lattice thermal conductivity (κ_L) is averaged over the three crystalline directions. $\kappa_p^{3,4ph}$ represents lattice thermal conductivity considering quartic anharmonic phonon renormalization (APRN) and four-phonon (4ph) interactions.

The influence of SCPH is crucial, as evidenced by

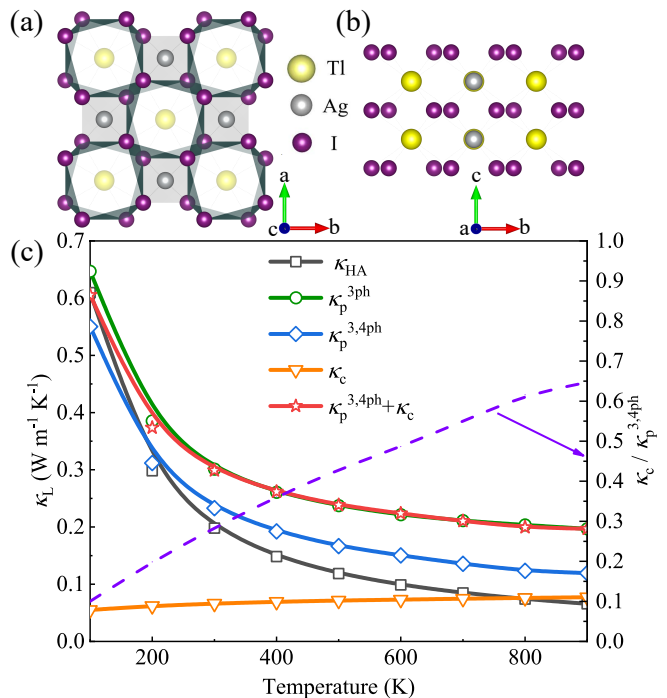


FIG. 1. The crystal structure of the conventional cell of TlAgI₂ is depicted, containing 16 atoms. The top view (a) and side view (b) along the crystallographic c -axis and a -axis are shown. (c) “HA” denotes the harmonic approximation. $\kappa_p^{3,4ph}$ represents lattice thermal conductivity, considering quartic anharmonic phonon renormalization (APRN) and four-phonon (4ph) interactions. κ_c is the contribution of the off-diagonal terms from the Wigner distribution. Thallium (Tl), silver (Ag), and iodine (I) atoms are represented by yellow, gray, and purple colors, respectively. The right vertical axis indicates the ratio of $\kappa_c / \kappa_p^{3,4ph}$. The lattice thermal conductivity (κ_L) is averaged over the three coordinates.

the contrast between HA and κ_p^{3ph} , highlighting a pronounced temperature effect on phonons. Compared with the κ_p^{3ph} value of $0.30 \text{ W m}^{-1} \text{ K}^{-1}$, $\kappa_p^{3,4ph}$ decreases to $0.23 \text{ W m}^{-1} \text{ K}^{-1}$ at 300 K due to additional 4ph scattering. However, when considering the contribution of the off-diagonal term (κ_c), the total lattice thermal conductivity increases to $0.30 \text{ W m}^{-1} \text{ K}^{-1}$, constituting $\kappa_p^{3,4ph} + \kappa_c$. Interestingly, the contribution of coherent phonons κ_c grows significantly with increasing temperature. At room temperature, the lattice thermal conductivity of κ_p^{3ph} aligns with that of $\kappa_p^{3,4ph} + \kappa_c$.

Subsequently, we delve into the frequency-resolved analysis (filled region) and cumulative trends (solid lines) of κ_L at 300 K to further scrutinize the microscopic mechanisms of phonon vibrations leading to low κ_L , as illustrated in Fig. 2(a). The κ_L spectrum and the cumulative κ_L with respect to frequency reveal that the primary contributors to κ_L are the phonon branches within the 2-4 meV range, affirming the validity of our 4ph scattering calculation. At the same time, we find that acoustic phonons below 4 meV are the main contribution to the

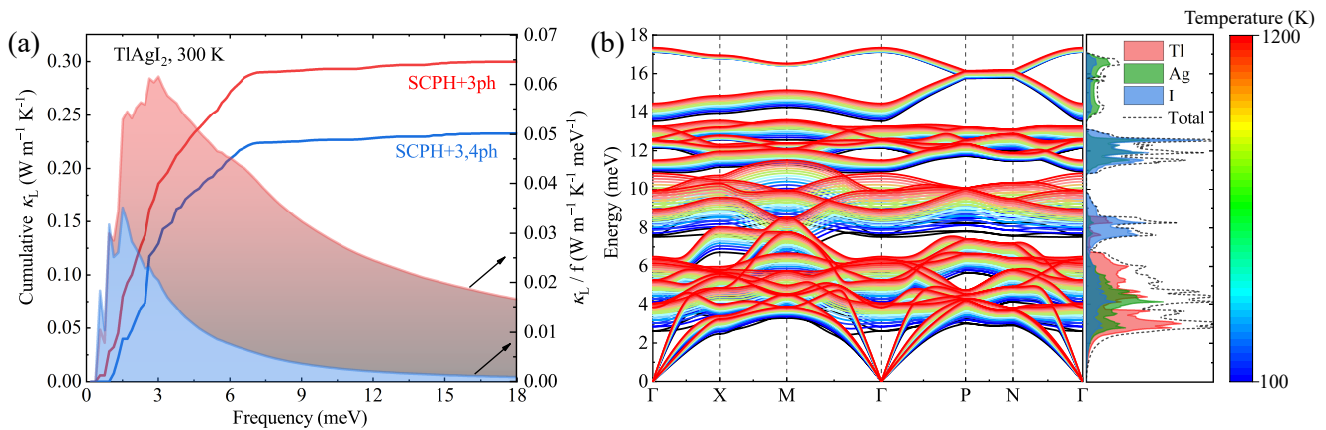


FIG. 2. (a) The frequency-resolved κ_L represented by the filled area below the lines, and the cumulative κ_L spectrum, indicated by the line. The methods are SCPH+3ph (red) and SCPH+3,4ph (blue) for TlAgI₂ material at 300 K, respectively. (b) The temperature-dependent colourful phonon spectrum for TlAgI₂ from T = 100 K to 1200 K using SCPH. The black line at T = 0 K denotes the harmonic approximation (HA). The element-decomposed density of states (PDOS) are shown in the red, green, and blue colors representing thallium (Tl), silver (Ag), and iodine (I) atoms. Total density of state is illustrated in dotted line.

lattice thermal conductivity, no matter the κ_p^{3ph} (red line) and $\kappa_p^{3,4ph}$ (blue line).

The temperature-dependent phonon dispersion unquestionably reveals the stiffening of both acoustic and optical branches with increasing temperature probably originating with weakly coupling between high-frequency optical phonons and overdamped acoustic phonons ($I_{\lambda\lambda_1}$ is positive as mentioned in Eq. (4)), as depicted in Fig. 2(b). The vibrational spectra of Tl atoms predominantly occupy the 2-4 meV regime, exerting significant influence on thermal transport as evidenced by the atom-projected phonon density of states (PDOS). It is also affirmed that the vibrations of Tl atoms serve as the primary scattering channel. Moreover, the strongly inter-linked phonon branches within the low-frequency range of 4-5 meV are anticipated to establish a substantial phonon-phonon scattering channel for both acoustic and low-frequency optical modes [48].

Finally, and perhaps most crucially, the outermost layer of Tl comprises three electrons, including $6s^2$ and $6p^1$. Theoretically, the valence states can be monovalent, divalent, and trivalent. Conversely, Ag possesses only one electron in the outermost layer, $5p^1$. This electron likely transfers to I, forming a stable ionic bond. Consequently, Tl can contribute only one valence electron to I, leaving a $6s^2$ lone pair electron. The Bader charge, detailed in Table SII in the Supplemental Materials, further supports this. As a result, the compound exhibits the following valence state: $Tl^{1+}Ag^{1+}(I^{1-})_2$.

The monovalent Tl in the TlAgI₂ system [47] with a $6s^2$ lone pair, exhibits overlapping wave functions of the lone electron pair with nearby valence electrons. This overlap causes a nonlinear repulsive electrostatic force as atoms approach each other, leading to off-centering

of the atoms. The interaction of the lone electron pair originating from the Tl 6s orbital with adjacent atoms induces bond anharmonicity and significantly reduces κ_L [26, 47, 49–51].

All available three-phonon (3ph) and four-phonon (4ph) scattering rates are depicted in Fig. 3(a). At the same temperature, the relationship of scattering rates (SR) can be expressed as $SR_{4ph} \geq SR_{3ph}$, indicating that 4ph scattering is not negligible in this system. Furthermore, scattering rates increase with temperature. Therefore, by including 4ph scattering, the lattice thermal conductivity is generally smaller than when considering only 3ph scattering, resulting in lower κ_L with increasing temperature.

Fig. 3(b) displays the absorption and emission processes of the 3ph and 4ph as a function of frequency at 300 K. For the 3ph scattering, we consider the phonon splitting ($\lambda \rightarrow \lambda_1 + \lambda_2$) and combination ($\lambda + \lambda_1 \rightarrow \lambda_2$). In the case of 4ph, we count for phonon splitting ($\lambda \rightarrow \lambda_1 + \lambda_2 + \lambda_3$), combination ($\lambda + \lambda_1 + \lambda_2 \rightarrow \lambda_3$), as well as redistribution ($\lambda + \lambda_1 \rightarrow \lambda_2 + \lambda_3$) processes. In the low-frequency region dominated by acoustic modes, 3ph combination is stronger than the splitting situation, while the redistribution process of 4ph is dominant. However, in the high-frequency region dominated by optical modes, the splitting process of 3ph becomes more important. For 4ph scattering, the splitting course dominates the scattering process and has the same order as the redistribution process. A similar phenomenon was observed in the case of the halide perovskite material CsPbBr₃ [32].

The phonon phase space at different temperatures for 3ph and 4ph interactions reveals a strong temperature dependence, particularly for 4ph, as illustrated in Fig. 3(c). The phase space of both 3ph and 4ph scattering increases

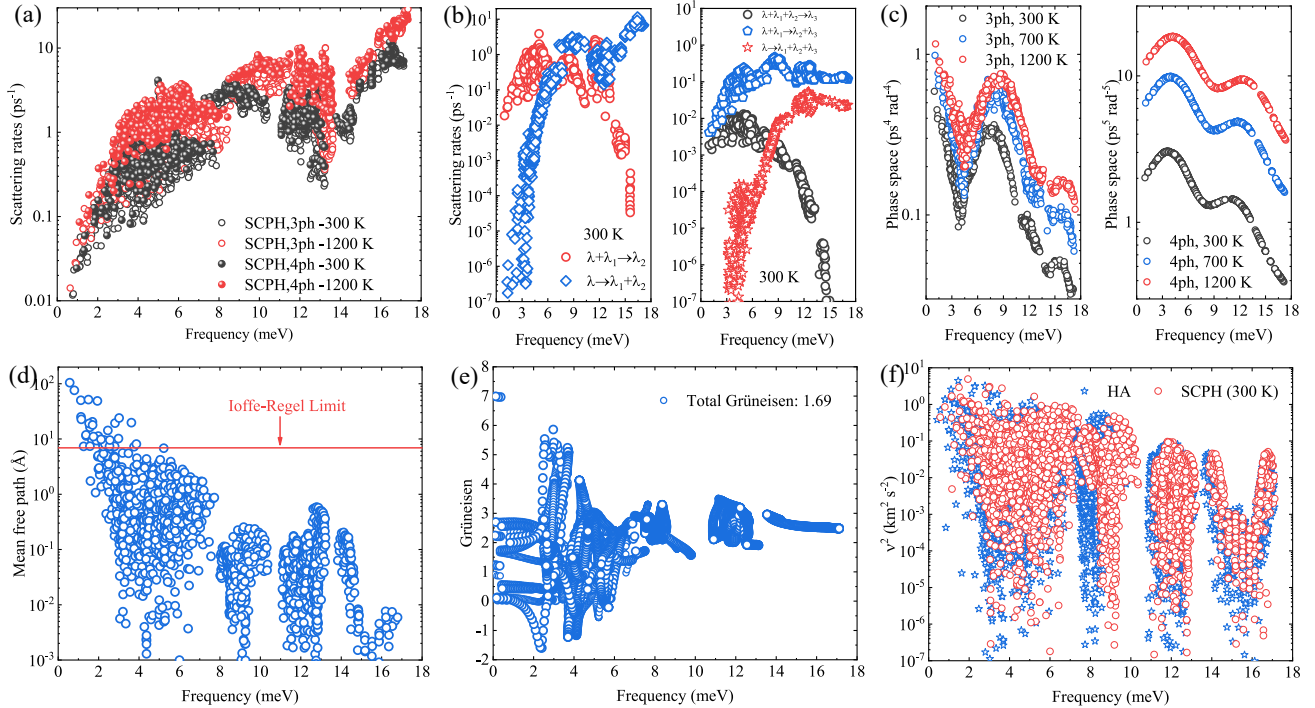


FIG. 3. Thermal transport mechanism analysis of ultralow κ_L of TlAgI_2 . (a) Phonon-phonon scattering rates of 3ph and 4ph at both 300 K and 1200 K. (b) Description of the decomposed scattering of 3ph and 4ph into splitting, reconstruction, and combination processes. (c) Illustration of the phonon scattering phase space of 3ph and 4ph. (d) The mean free path of phonons with the Ioffe-Regel Limit [52] at 300 K. (e) The Grüneisen parameter at 300 K. (f) The square of the phonon group velocity v^2 in the harmonic approximation and anharmonic phonon renormalization at 300 K.

as the temperature rising from 300 K to 700 K and 1200 K. It is important to note that the units of phase space for 3ph and 4ph are different, preventing a direct comparison between them [53].

We observed that crystalline materials with an antibonding state and bonding hierarchy exhibit a coexistence of population phonons and coherent phonons. Coherent phonons are likely to manifest in the presence of complex crystals [27], which require a large unit cell with numerous closely spaced phonon branches, strong anharmonicity (where phonon linewidths exceed interbranch spacings) [54], and phonons below the Ioffe-Regel Limit (mean free path is around the interatomic spacing) contributing to heat transport due to their wavelike ability to interfere and tunnel [55], as depicted in Fig. 3(d). Given that most mean free paths are smaller than the minimum atomic distance, known as the Ioffe-Regel Limit, it suggests that κ_c is likely important in TlAgI_2 [55].

To deepen our understanding of the physical mechanism behind the ultralow κ_L and the significance of anharmonicity, we calculate the Grüneisen parameter, as illustrated in Fig. 3(e). The extent of anharmonicity is typically measured by the Grüneisen parameters (γ). In the top panel of Fig. 3(e), relatively large values of γ are observed in intertwined portions of the acoustic and optical branches regime at 300 K, confirming stronger scat-

tering within the frequency range of 2 to 4 meV. This is closely linked to the heavy atomic mass of the Tl element and the bonding hierarchy. Moreover, TlAgI_2 exhibits substantial anharmonicity with a total Grüneisen value of 1.69, indicating more anharmonicity than the PbTe value of 1.45 [56]. Fig. 3(f) demonstrates the temperature effect on v^2 , where v represents the group velocity. We observe a low speed of sound at 300 K for TlAgI_2 , stemming from the heavy atomic mass of the Tl element and the vibration resistance, as indicated by the renormalized phonon dispersions at finite temperature.

In Fig. 4(a), the electronic band structure and projective density of states for different elemental orbitals of TlAgI_2 are presented. TlAgI_2 is identified as an indirect bandgap semiconductor, where the conduction band minimum (CBM) is located at the M point, and the valence band maximum (VBM) is situated at the Γ to X high symmetry line. The computed bandgap using the PBEsol functional is 1.55 eV, consistent with the findings from the Material Project database mp-27801. TlAgI_2 is characterized as a wide bandgap semiconductor, a common feature in high temperature thermoelectric semiconductor materials, such as half-heusler alloys $\text{FeNb}_{0.88}\text{Hf}_{0.12}\text{Sb}$ [57]. Specifically, the CBM is predominantly contributed by the Tl atom's 6p orbital, while the VBM is almost entirely attributed to the Ag 4d and I 5p

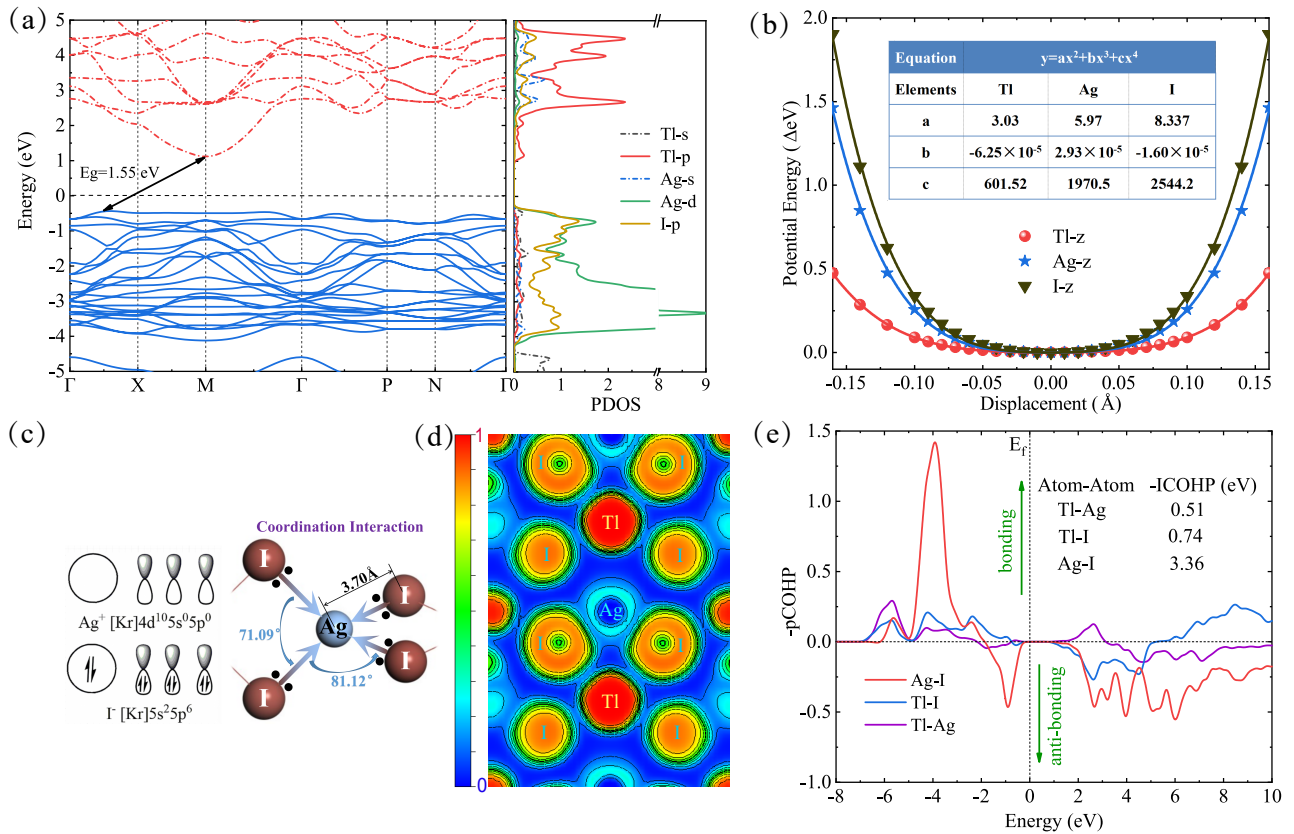


FIG. 4. Electrical transport mechanism analysis of TlAgI₂. (a) The electron energy band and projective density of states for different elemental orbitals in TlAgI₂. (b) The potential energy versus displacement along crystallographic *z*-direction of TlAgI₂ in conventional cell. (c) The coordination states of silver and iodine, with brown and blue atom representing Ag and I, respectively. Bond angles are 81.12° and 71.09° (The symmetric position possesses same bond Angle), all the bond lengths are 3.70 \AA . (d) The 2D electron location function (ELF) of TlAgI₂. (e) The calculated projected crystal orbital Hamiltonian population (pCOHP) analysis for the Tl-Ag, Tl-I, and Ag-I of TlAgI₂, where the negative values of -pCOHP represent bonding states, and the positive values indicate anti-bonding states. The energy is shifted to the Fermi level at 0 eV.

orbitals.

The conduction band near the Fermi energy level exhibits pronounced valleys, while the valence band appears notably flat. In semiconductors with highly asymmetric bands near the Fermi energy, there is a substantial difference in the density of states between electrons and holes. When the concentration of one type of carrier significantly exceeds that of the other, the detrimental impact of the bipolar effect on the Seebeck coefficient can be effectively mitigated [58]. Simultaneously, a higher valence density of states enhances the material's responsiveness to the effects of thermoelectric conversion.

For an in-depth understanding of atomic-level dynamics, we computed potential energy curves by displacing atoms along the *z*-direction relative to their static equilibrium positions at the Γ point. As depicted in Fig. 4(b), Ag and I atoms are confined in steep potential wells, while the Tl atom resides in a flat potential well. This suggests that the Tl atom can readily oscillate within the surrounding hollow cage with a large amplitude. The

electrostatic repulsion between the localized electrons of Tl and the neighboring atoms likely induces significant vibrations of Tl. Consequently, chemical bonds various strengths coexist in the system, the pronounced mismatch in their vibrational modes impedes phonon propagation. This increased anharmonicity effectively reduces the κ_L [59]. The flat potential well of Tl is consistent with its large Atomic Displacement Parameter (ADP). The loose bonding between Tl and other elements, coupled with electrostatic repulsion between the localized electrons (lone pair $6s^2$) of Tl and the surroundings, plausibly drives substantial displacement of Tl, leading to a large ADP along the *c*-axis, as illustrated in the Supplemental Materials FIG. S2.

The schematic of coordination compounds Ag¹⁺I¹⁻, illustrated in Fig. 4(c), reveals the unique electron configurations of the components. The I¹⁻ anion adheres to the eight-electron rule, possessing four lone pair electrons. Conversely, the Ag¹⁺ cation displays unpaired 5s and 5p orbitals. This distinctive electron arrangement leads to

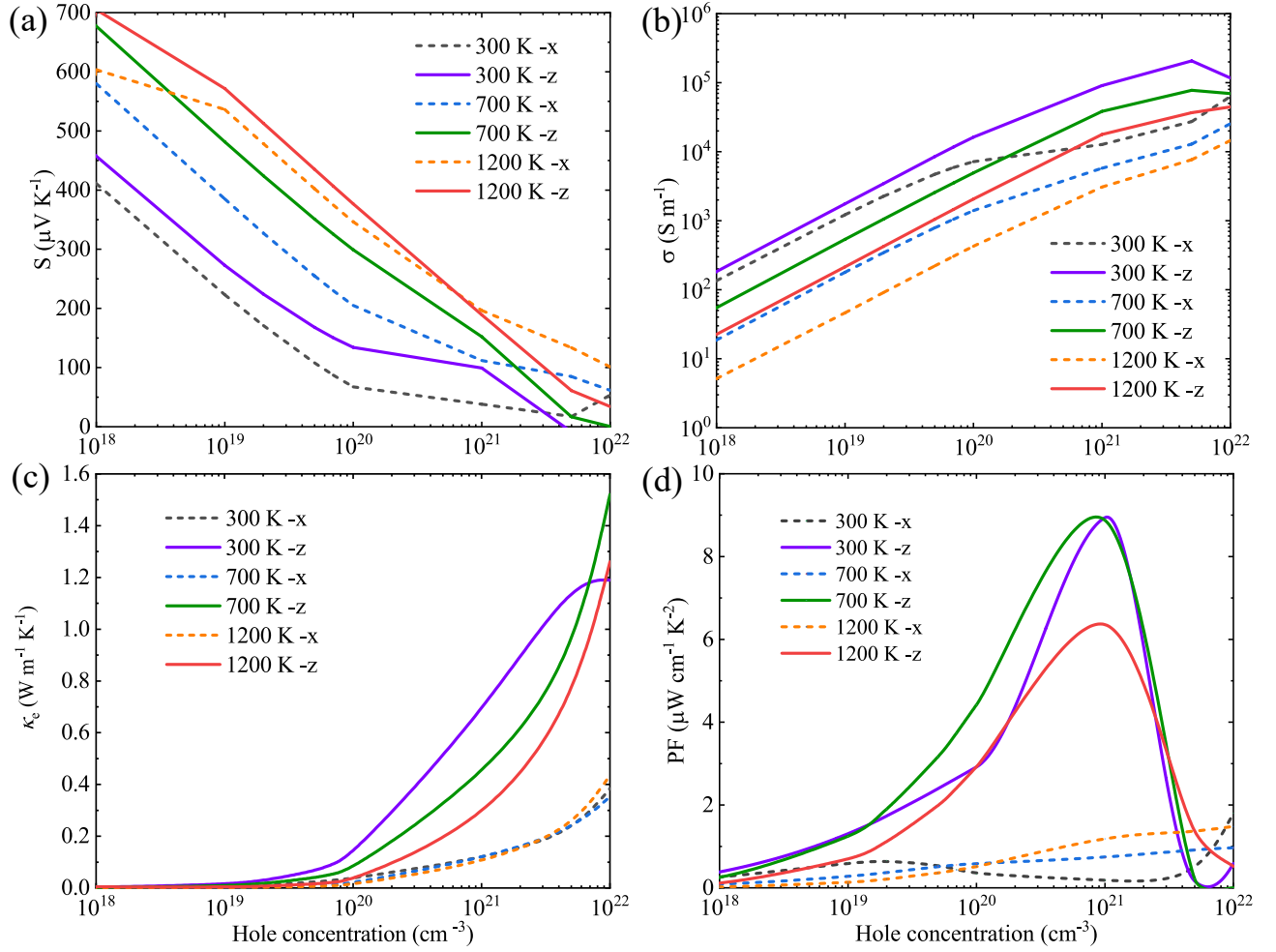


FIG. 5. The carrier transport performance of TlAgI₂. (a) The Seebeck coefficient, (b) Electrical conductivity, (c) Electronic thermal conductivity, and (d) Power factor PF ($PF = S^2\sigma$) of the p-type with x -axis and z -axis, respectively.

the formation of the coordination bond $I^{1-}-Ag^{1+}$, aligning with the Projected Density of States (PDOS) where p orbitals of Ag and I significantly contribute to the valence band. The coordination interactions are strengthened by similar energy levels and matching symmetry of the orbitals involved in bond formation. This results in the establishment of a stable coordination complex, AgI, where the I^{1-} anion acts as a ligand, and the Ag^{1+} cation serves as the central metal ion. Such coordination bonds play a crucial role in electrical transport processes, facilitating the transfer of electrons between the ligand and the central metal ion [26].

Furthermore, the exceedingly weak bonding between Tl and I, particularly evident around the Tl element and the delocalization of Tl, as depicted in Fig. 4(d), suggests a spherical charge density due to the electron lone pair of Tl (refer to Fig. 2(b)). This implies that the interactions between Tl and the surrounding Ag and I atoms are primarily electrostatic. With a combination of ionic bonding, covalent bonding, and coordination interaction,

the hierarchical bonding and mismatched bond energies result in strong anharmonic interactions, especially below the Fermi level. Due to the strong electron separability at the top of the valence band, the robust coordination interactions of Ag and I contribute to a high density of states effective mass [20, 21].

Fig. 4(e) illustrates the projected crystal orbital Hamiltonian population (pCOHP) analysis. The Ag-I interaction exhibits strong bonding states, with antibonding states below the Fermi level in the electronic structure resulting from the interactions between silver 4d and iodine 5p orbitals. This weakens the bond and induces strong phonon anharmonicity. In contrast, Tl-Ag and Tl-I interactions display weak bonding states. Evidently, Tl atoms are loosely bound to other atoms, attributed to the lone pair and rattling vibration mode. The value of -ICOHP represents the integrals from -infinity to the Fermi level of COHP, signifying the ability to form bonds between different atoms, consistent with the 2D electron location function shown in Fig. 4(d).

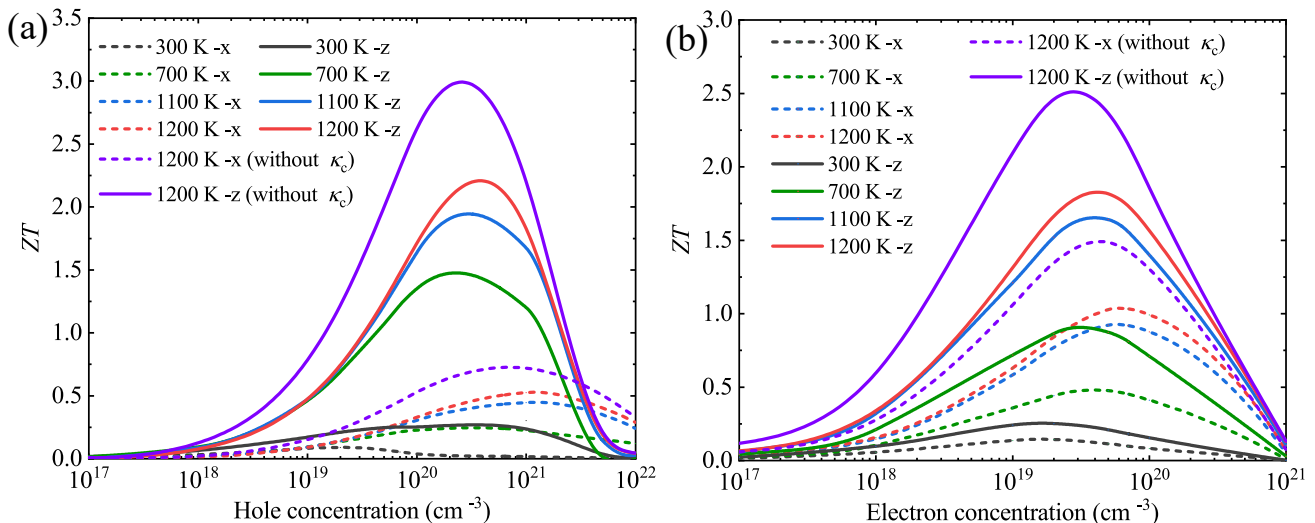


FIG. 6. The calculated thermoelectric figure of merit (ZT) with the lattice thermal conductivity (κ_L) originating from both phonon (κ_p) and coherent (κ_c) contributions ($\kappa_L = \kappa_p^{3,4ph} + \kappa_c$) for (a) p-type and (b) n-type TlAgI₂ at temperatures of 300 K, 700 K, 1100 K, and 1200 K. A comparison is provided by calculating κ_p only for TlAgI₂ at 1200 K for both p-type and n-type carriers.

The hole transport performance for p-type TlAgI₂ is depicted in Fig. 5. Observations reveal that the Seebeck coefficient S decreases with increasing carrier concentration n of holes at the same temperature, while S increases with increasing T at the same n . The electrical conductivity σ of p-type TlAgI₂ shows a positive correlation with the carrier concentration n and a negative correlation with the temperature T . Notably, p-type TlAgI₂ exhibits a larger S due to high energy band asymmetry and a wide bandgap that counteracts the bipolar effect, especially at high temperatures, as illustrated in Fig. 4(a). The conductivity σ is influenced by the carrier concentration n and inversely proportional to the temperature T . The former is attributed to the increasing concentration n , contributing to the conductivity, while the latter is due to the boosting of the electron-phonon interaction scattering rate with increasing temperature.

In general, the electrical conductivity σ and electronic thermal conductivity κ_e exhibit a similar trend with the increase in hole concentration, as depicted in Fig. 5(b) and Fig. 5(c), consistent with the Wiedemann-Franz law ($\kappa_e = L\sigma T$) [60]. Due to the coexistence of relatively large Seebeck coefficient S and σ , a high thermoelectric power factor (PF) is achieved, for instance, 8.94 $\mu\text{W cm}^{-1} \text{K}^{-2}$ at 300 K in the z -direction at a hole concentration (n_h) of 10²¹ cm⁻³. Notably, there is a positive correlation between the bandgap and the temperature at the highest ZT value [12]. Considering the bandgap of TlAgI₂ is 1.55 eV, which is relatively large, we tentatively selected the highest temperature to be 1200 K, commonly used for high-temperature thermoelectric materials. It is observed that the highest power factor occurs at a hole doping concentration of 10²¹. The electrical transport

performance for n-type TlAgI₂ is presented in the Supplemental Material and shows lower performance.

As depicted in Fig. 6, the ZT values for p-type doping are relatively high, reaching 2.20, whereas for n-type doping, it is only 1.82. The highest ZT for n-type doping is observed at a carrier concentration of 2×10^{19} at 1200 K, and the most reasonable concentration for p-type doping is 2×10^{20} at 1200 K. An interesting observation is that the ZT without considering κ_c can be enhanced from 2.20 to 3.00, even though the value of κ_c is only 0.08 $\text{W m}^{-1} \text{K}^{-1}$ (as shown in Supplemental Material TABLE. SI.) at 1200 K. Therefore, it is crucial to consider κ_c when calculating the ZT to avoid overestimating the thermoelectric performance, especially for materials with low thermal conductivity [24].

Based on our investigation of existing wide bandgap thermoelectric materials, including pure semiconductors and doping-modified multifunctional semiconductor materials illustrated in Fig. 7, it is noteworthy that most of the thermoelectric materials with a bandgap exceeding 1.0 eV exhibit ZT values below 1.0. A notable exception is Cu₂Se, where doping with sulfur element elevates the ZT from 1.4 to 2.0. Consequently, our findings establish that the ZT value of 2.20 for TlAgI₂ takes a leading position in the bandgap range of 1.0 eV to 3.5 eV. This suggests that TlAgI₂ holds significant promise as a potential thermoelectric material at high temperatures. Furthermore, there is potential to enhance the ZT value through doping. Therefore, it is advisable to explore the application of wide bandgap semiconductors in high-temperature thermoelectric materials.

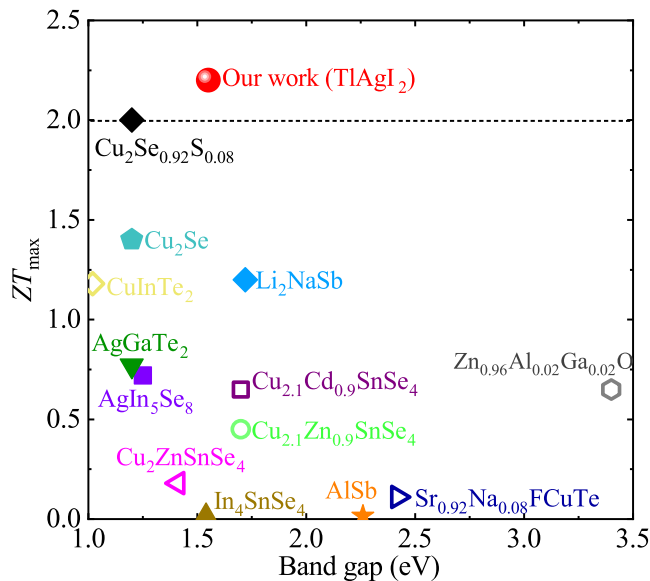


FIG. 7. Some bandgap and thermoelectric data from experiments and calculations at reaching ZT_{max} temperatures. In_4SnSe_4 [61], Li_2NaSb [16], AgIn_5Se_8 [62], $\text{Cu}_2\text{ZnSnSe}_4$ [15], CuInTe_2 [63], $\text{Cu}_{2.1}\text{Cd}_{0.9}\text{SnSe}_4$ and $\text{Cu}_{2.1}\text{Zn}_{0.9}\text{SnSe}_4$ [18], $\text{Sr}_{0.92}\text{Na}_{0.08}\text{FCuTe}$ and $\text{Sr}_{0.94}\text{Na}_{0.06}\text{FCuTe}$ [64], AlSb [65], Cu_2Se and $\text{Cu}_2\text{Se}_{0.92}\text{S}_{0.08}$ [17], AgGaTe_2 [66], $\text{Zn}_{0.96}\text{Al}_{0.02}\text{Ga}_{0.02}\text{O}$ [67].

IV. CONCLUSIONS

In summary, we employed first-principles calculations, the self-consistent phonon (SCPH) theory, and Boltzmann transport equations to investigate the thermal and electrical transport properties of TlAgI_2 . The results revealed distinctive effects of quartic anharmonicity and coherent phonons on lattice thermal conductivity. Key findings include:

(i) The study highlighted the significant contributions of four-phonon processes, anharmonicity phonon renormalization, and coherent phonons in achieving ultralow thermal conductivity. These factors are crucial in theoretical predictions for high thermoelectric performance materials. (ii) The observed low thermal conductivity in TlAgI_2 is attributed to antibonding states of Ag 4d and I 5p orbitals below the Fermi level, along with the bonding hierarchy of ionic, covalent, and coordination interactions. Strong Ag-I coordination interactions lead to a large valence band state density. Favorable electrical transport properties are linked to high energy band asymmetry and a wide bandgap, countering bipolar effects, especially at high temperatures. (iii) TlAgI_2 emerges as a potential candidate for thermoelectric applications due to its ultralow thermal conductivity and favorable electrical transport properties. This research contributes to advancing our understanding of the thermal and electrical properties of TlAgI_2 , offering guidance

for the exploration of materials with wide bandgaps for high-temperature thermoelectric applications.

ACKNOWLEDGMENTS

This work is sponsored by the Key Research and Development Program of the Ministry of Science and Technology (No.2023YFB4604100). We acknowledge the support from the National Natural Science Foundation of China (No.12104356 and No.52250191, No.22103099), the Opening Project of Shanghai Key Laboratory of Special Artificial Microstructure Materials and Technology (No.Ammt2022B-1), and the Fundamental Research Funds for the Central Universities. W. Shi acknowledges the support from the Guangzhou Science and Technology Plan Project (202201011155). We also acknowledge the support by HPC Platform, Xi'an Jiaotong University.

[†] E-mail: zhibin.gao@xjtu.edu.cn

- [1] Jian He and Terry M Tritt, “Advances in thermoelectric materials research: Looking back and moving forward,” *Science* **357**, eaak9997 (2017).
- [2] G Jeffrey Snyder and Eric S Toberer, “Complex thermoelectric materials,” *Nat. Mater.* **7**, 105–114 (2008).
- [3] Pierre FP Poudeu, Jonathan D’Angelo, Adam D Downey, Jarrod L Short, Timothy P Hogan, and Mercouri G Kanatzidis, “High thermoelectric figure of merit and nanostructuring in bulk p-type $\text{Na}_{1-x}\text{Pb}_m\text{Sb}_y\text{Te}_{m+2}$,” *Angew. Chem. Int. Ed.* **45**, 3835–3839 (2006).
- [4] E. A. Albanesi, C. M. I. Okoye, C. O. Rodriguez, E. L. Peltzer y Blanca, and A. G. Petukhov, “Electronic structure, structural properties, and dielectric functions of IV-VI semiconductors: PbSe and PbTe ,” *Phys. Rev. B* **61**, 16589–16595 (2000).
- [5] Bed Poudel, Qing Hao, Yi Ma, Yucheng Lan, Austin Minnich, Bo Yu, Xiao Yan, Dezhi Wang, Andrew Muto, Daryoosh Vashaee, Xiaoyuan Chen, Junming Liu, Mildred S. Dresselhaus, Gang Chen, and Zhifeng Ren, “High-thermoelectric performance of nanostructured bismuth antimony telluride bulk alloys,” *Science* **320**, 634–638 (2008).
- [6] Peigen Li, Teng Ding, Junqin Li, Chunxiao Zhang, Yubo Dou, Yu Li, Lipeng Hu, Fusheng Liu, and Chaozhuo Zhang, “Positive effect of Ge vacancies on facilitating band convergence and suppressing bipolar transport in GeTe-based alloys for high thermoelectric performance,” *Adv. Funct. Mater.* **30**, 1910059 (2020).
- [7] Zhiwei Chen, Xinyue Zhang, Jie Ren, Zezhu Zeng, Yue Chen, Jian He, Lidong Chen, and Yanzhong Pei, “Leveraging bipolar effect to enhance transverse thermoelectricity in semimetal Mg_2Pb for cryogenic heat pumping,” *Nat. Commun.* **12**, 3837 (2021).
- [8] Gaia Germanese, Federico Paolucci, Giampiero Marchegiani, Alessandro Braggio, and Francesco Giazotto, “Bipolar thermoelectric josephson engine,” *Nat. Nanotechnol.* **17**, 1084–1090 (2022).

- [9] Yanzhong Pei, Heng Wang, and GJ Snyder, “Thermoelectric materials: band engineering of thermoelectric materials,” *Adv. Mater.* **24**, 6124–6124 (2012).
- [10] Khang Hoang, SD Mahanti, and Mercuri G Kanatzidis, “Impurity clustering and impurity-induced bands in PbTe-, SnTe-, and GeTe-based bulk thermoelectrics,” *Phys. Rev. B* **81**, 115106 (2010).
- [11] Yanzhong Pei, Nicholas A. Heinz, and G. Jeffrey Snyder, “Alloying to increase the band gap for improving thermoelectric properties of Ag₂Te,” *J. Mater. Chem.* **21**, 18256–18260 (2011).
- [12] Yu Xiao and Li-Dong Zhao, “Seeking new, highly effective thermoelectrics,” *Science* **367**, 1196–1197 (2020).
- [13] Li Dong Zhao, Shih Han Lo, Yongsheng Zhang, Hui Sun, Gangjian Tan, Ctirad Uher, C. Wolverton, Vinayak P. Dravid, and Mercuri G. Kanatzidis, “Ultralow thermal conductivity and high thermoelectric figure of merit in SnSe crystals,” *Nature* **508**, 373–377 (2014).
- [14] Li-Dong Zhao, Gangjian Tan, Shiqiang Hao, Jiaqing He, Yanling Pei, Hang Chi, Heng Wang, Shengkai Gong, Huibin Xu, Vinayak P. Dravid, Ctirad Uher, G. Jeffrey Snyder, Chris Wolverton, and Mercuri G. Kanatzidis, “Ultrahigh power factor and thermoelectric performance in hole-doped single-crystal SnSe,” *Science* **351**, 141–144 (2016).
- [15] Min-Ling Liu, I-Wei Chen, Fu-Qiang Huang, and Li-Dong Chen, “Improved thermoelectric properties of Cu-doped quaternary chalcogenides of Cu₂CdSnSe₄,” *Adv. Mater.* **21**, 3808–3812 (2009).
- [16] Guangzong Xing, Jifeng Sun, Yuwei Li, Xiaofeng Fan, Weitao Zheng, and David J. Singh, “Electronic fitness function for screening semiconductors as thermoelectric materials,” *Phys. Rev. Mater.* **1**, 065405 (2017).
- [17] Ping Lu, Huili Liu, Xun Yuan, Fangfang Xu, Xun Shi, Kunpeng Zhao, Wujie Qiu, Wenqing Zhang, and Lidong Chen, “Multiformity and fluctuation of Cu ordering in Cu₂Se thermoelectric materials,” *J. Mater. Chem. A* **3**, 6901–6908 (2015).
- [18] XY Shi, FQ Huang, ML Liu, and LD Chen, “Thermoelectric properties of tetrahedrally bonded wide-gap stannite compounds Cu₂ZnSn_{1-x}In_xSe₄,” *Appl. Phys. Lett.* **94**, 122103 (2009).
- [19] Minling Liu, Fuqiang Huang, Lidong Chen, and I-W. Chen, “A wide-band-gap p-type thermoelectric material based on quaternary chalcogenides of Cu₂ZnSnQ₄ (Q=S,Se),” *Appl. Phys. Lett.* **94**, 202103 (2009).
- [20] Paribesh Acharyya, Koushik Pal, Abdul Ahad, Debatam Sarkar, Kewal Singh Rana, Moinak Dutta, Ajay Soni, Umesh V Waghmare, and Kanishka Biswas, “Extended antibonding states and phonon localization induce ultralow thermal conductivity in low dimensional metal halide,” *Adv. Funct. Mater.* **33**, 2304607 (2023).
- [21] Koushik Pal, Jiangang He, and C Wolverton, “Bonding hierarchy gives rise to high thermoelectric performance in layered zintl compound BaAu₂P₄,” *Chem. Mater.* **30**, 7760–7768 (2018).
- [22] Biao Wan, Zhibin Gao, Xiaochen Huang, Yuqian Yang, Liangchao Chen, Qianqian Wang, Chao Fang, Weixia Shen, Yuewen Zhang, Hongan Ma, Huiyang Gou, Xiaopeng Jia, and Zhuangfei Zhang, “Bonding Heterogeneity Inducing Low Lattice Thermal Conductivity and High Thermoelectric Performance in 2D CdTe₂,” *ACS Appl. Mater. Sci.* **5**, 9549–9558 (2022).
- [23] Yixiu Luo, Xiaolong Yang, Tianli Feng, Jingyang Wang, and Xiulin Ruan, “Vibrational hierarchy leads to dual-phonon transport in low thermal conductivity crystals,” *Nat. Commun.* **11**, 2554 (2020).
- [24] Zhen Tong, Alessandro Pecchia, ChiYung Yam, Traian Dumitrica, and Thomas Frauenheim, “Glass-like Transport Dominates Ultralow Lattice Thermal Conductivity in Modular Crystalline Bi₄O₄SeCl₂,” *Nano Lett.* **23**, 9468–9473 (2023).
- [25] Wujie Qiu, Lili Xi, Ping Wei, Xuezhi Ke, Jihui Yang, and Wenqing Zhang, “Part-crystalline part-liquid state and rattling-like thermal damping in materials with chemical-bond hierarchy,” *Proc. Natl. Acad. Sci.* **111**, 15031–15035 (2014).
- [26] Eric J Skoug and Donald T Morelli, “Role of lone-pair electrons in producing minimum thermal conductivity in nitrogen-group chalcogenide compounds,” *Phys. Rev. Lett.* **107**, 235901 (2011).
- [27] Michele Simoncelli, Nicola Marzari, and Francesco Mauri, “Unified theory of thermal transport in crystals and glasses,” *Nat. Phys.* **15**, 809–813 (2019).
- [28] Gaston Kané, Michele Lazzeri, and Francesco Mauri, “Zener tunneling in the electrical transport of quasimetallic carbon nanotubes,” *Phys. Rev. B* **86**, 155433 (2012).
- [29] NR Werthamer, “Self-consistent phonon formulation of anharmonic lattice dynamics,” *Phys. Rev. B* **1**, 572 (1970).
- [30] Alberto Debernardi, Stefano Baroni, and Elisa Molinari, “Anharmonic phonon lifetimes in semiconductors from density-functional perturbation theory,” *Phys. Rev. Lett.* **75**, 1819–1822 (1995).
- [31] Zhibin Gao, Fang Tao, and Jie Ren, “Unusually low thermal conductivity of atomically thin 2D tellurium,” *Nanoscale* **10**, 12997–13003 (2018).
- [32] Xiaoying Wang, Zhibin Gao, Guimei Zhu, Jie Ren, Lei Hu, Jun Sun, Xiangdong Ding, Yi Xia, and Baowen Li, “Role of high-order anharmonicity and off-diagonal terms in thermal conductivity: A case study of multi-phase CsPbBr₃,” *Phys. Rev. B* **107**, 214308 (2023).
- [33] P. Souvatzis, O. Eriksson, M. I. Katsnelson, and S. P. Rudin, “Entropy driven stabilization of energetically unstable crystal structures explained from first principles theory,” *Phys. Rev. Lett.* **100**, 095901 (2008).
- [34] Ion Errea, Matteo Calandra, and Francesco Mauri, “Anharmonic free energies and phonon dispersions from the stochastic self-consistent harmonic approximation: Application to platinum and palladium hydrides,” *Phys. Rev. B* **89**, 064302 (2014).
- [35] Terumasa Tadano and Shinji Tsuneyuki, “Self-consistent phonon calculations of lattice dynamical properties in cubic SrTiO₃ with first-principles anharmonic force constants,” *Phys. Rev. B* **92**, 054301 (2015).
- [36] Yi Xia, Vinay I. Hegde, Koushik Pal, Xia Hua, Dale Gaines, Shane Patel, Jiangang He, Muratahan Aykol, and Chris Wolverton, “High-throughput study of lattice thermal conductivity in binary rocksalt and zinc blende compounds including higher-order anharmonicity,” *Phys. Rev. X* **10**, 041029 (2020).
- [37] G. Kresse and J. Furthmüller, “Efficient iterative schemes for *ab initio* total-energy calculations using a plane-wave basis set,” *Phys. Rev. B* **54**, 11169–11186 (1996).
- [38] P. E. Blöchl, “Projector augmented-wave method,” *Phys. Rev. B* **50**, 17953–17979 (1994).

- [39] G. Kresse and D. Joubert, “From ultrasoft pseudopotentials to the projector augmented-wave method,” *Phys. Rev. B* **59**, 1758–1775 (1999).
- [40] Alex M Ganose, Junsoo Park, Alireza Faghaninia, Rachel Woods-Robinson, Kristin A Persson, and Anubhav Jain, “Efficient calculation of carrier scattering rates from first principles,” *Nat. Commun.* **12**, 2222 (2021).
- [41] Fei Zhou, Weston Nielson, Yi Xia, and Vidvuds Ozoliņš, “Lattice anharmonicity and thermal conductivity from compressive sensing of first-principles calculations,” *Phys. Rev. Lett.* **113**, 185501 (2014).
- [42] Fei Zhou, Weston Nielson, Yi Xia, and Vidvuds Ozoliņš, “Compressive sensing lattice dynamics. I. General formalism,” *Phys. Rev. B* **100**, 184308 (2019).
- [43] Fei Zhou, Babak Sadigh, Daniel Åberg, Yi Xia, and Vidvuds Ozoliņš, “Compressive sensing lattice dynamics. II. Efficient phonon calculations and long-range interactions,” *Phys. Rev. B* **100**, 184309 (2019).
- [44] Emmanuel J. Candes and Michael B. Wakin, “An introduction to compressive sampling,” *IEEE Signal Process. Mag.* **25**, 21–30 (2008).
- [45] Tianli Feng and Xiulin Ruan, “Quantum mechanical prediction of four-phonon scattering rates and reduced thermal conductivity of solids,” *Phys. Rev. B* **93**, 045202 (2016).
- [46] Leyla Isaeva, Giuseppe Barbalinardo, Davide Donadio, and Stefano Baroni, “Modeling heat transport in crystals and glasses from a unified lattice-dynamical approach,” *Nat. Commun.* **10**, 3853 (2019).
- [47] Manoj K Jana, Koushik Pal, Avinash Warankar, Pankaj Mandal, Umesh V Waghmare, and Kanishka Biswas, “Intrinsic rattler-induced low thermal conductivity in Zintl type TlInTe_2 ,” *J. Am. Chem. Soc.* **139**, 4350–4353 (2017).
- [48] Wenwen Lin, Jiangang He, Xianli Su, Xiaomi Zhang, Yi Xia, Trevor P. Bailey, Constantinos C. Stoumpos, Ganjian Tan, Alexander J. E. Rettie, Duck Young Chung, Vinayak P. Dravid, Ctirad Uher, Chris Wolverton, and Mercouri G. Kanatzidis, “Ultralow thermal conductivity, multiband electronic structure and high thermoelectric figure of merit in TlCuSe ,” *Adv. Mater.* **33**, 2104908 (2021).
- [49] Saikat Mukhopadhyay, David J Singh, and Thomas L Reinecke, “Ultralow thermal conductivity in Cs–Sb–Se compounds: lattice instability versus lone-pair electrons,” *Chem. Mater.* **32**, 8906–8913 (2020).
- [50] Ekashmi Rathore, Rinkle Juneja, Sean P Culver, Nicolo Minafra, Abhishek K Singh, Wolfgang G Zeier, and Kanishka Biswas, “Origin of ultralow thermal conductivity in n-type cubic bulk AgBiS_2 : soft Ag vibrations and local structural distortion induced by the Bi $6s^2$ lone pair,” *Chem. Mater.* **31**, 2106–2113 (2019).
- [51] DT Morelli, V Jovicic, and JP Heremans, “Intrinsically minimal thermal conductivity in cubic I–V–VI₂ semiconductors,” *Phys. Rev. Lett.* **101**, 035901 (2008).
- [52] NE Hussey, K Takenaka, and H Takagi, “Universality of the Mott–Ioffe–Regel limit in metals,” *Philos. Mag.* **84**, 2847–2864 (2004).
- [53] Tianli Feng, Lucas Lindsay, and Xiulin Ruan, “Four-phonon scattering significantly reduces intrinsic thermal conductivity of solids,” *Phys. Rev. B* **96**, 161201 (2017).
- [54] Yi Xia, Vidvuds Ozoliņš, and Chris Wolverton, “Microscopic mechanisms of glasslike lattice thermal transport in cubic $\text{Cu}_{12}\text{Sb}_4\text{S}_{13}$ tetrahedrites,” *Phys. Rev. Lett.* **125**, 085901 (2020).
- [55] Michele Simoncelli, Nicola Marzari, and Francesco Mauri, “Wigner formulation of thermal transport in solids,” *Phys. Rev. X* **12**, 041011 (2022).
- [56] Glen A Slack, “The thermal conductivity of nonmetallic crystals,” *Solid State Phys.* **34**, 1–71 (1979).
- [57] Chenguang Fu, Shengqiang Bai, Yintu Liu, Yunshan Tang, Lidong Chen, Xinbing Zhao, and Tiejun Zhu, “Realizing high figure of merit in heavy-band p-type half-Heusler thermoelectric materials,” *Nat. Commun.* **6**, 8144 (2015).
- [58] JJ Gong, AJ Hong, J Shuai, L Li, ZB Yan, ZF Ren, and J-M Liu, “Investigation of the bipolar effect in the thermoelectric material CaMg_2Bi_2 using a first-principles study,” *Phys. Chem. Chem. Phys.* **18**, 16566–16574 (2016).
- [59] Tongcai Yue, Yinchang Zhao, Jun Ni, Sheng Meng, and Zhenhong Dai, “Strong quartic anharmonicity, ultralow thermal conductivity, high band degeneracy and good thermoelectric performance in Na_2TlSb ,” *npj Comput Mater* **9**, 17 (2023).
- [60] M Jonson and GD Mahan, “Mott’s formula for the thermopower and the wiedemann-franz law,” *Phys. Rev. B* **21**, 4223 (1980).
- [61] Haonan Shi, Changrong Guo, Bingchao Qin, Guangtao Wang, Dongyang Wang, and Li-Dong Zhao, “A promising thermoelectrics In_4SnSe_4 with a wide bandgap and cubic structure composited by layered SnSe and In_4Se_3 ,” *J. Materiomics* **8**, 982–991 (2022).
- [62] JL Cui, YY Li, Y Deng, QS Meng, YL Gao, H Zhou, and YP Li, “Microstructure modulation responsible for the improvement in thermoelectric property of a wide-gap AgIn_5Se_8 semiconductor,” *Intermetallics* **31**, 217–224 (2012).
- [63] Ruiheng Liu, Lili Xi, Huili Liu, Xun Shi, Wenqing Zhang, and Lidong Chen, “Ternary compound CuInTe_2 : a promising thermoelectric material with diamond-like structure,” *Chem. Commun.* **48**, 3818–3820 (2012).
- [64] Yumei Jiang, Yuting Zhang, Juanjuan Xing, Yibin Hu, Xinxin Yang, Jiye Zhang, Kai Guo, and Jun Luo, “Assessment of the thermoelectric performance of layered semiconductor AgIn_5Se_8 with wide band-gap,” *J. Solid State Chem.* **299**, 122169 (2021).
- [65] AKM Ashiquzzaman Shawon and Soon-Chul Ur, “Mechanical and thermoelectric properties of bulk AlSb synthesized by controlled melting, pulverizing and subsequent vacuum hot pressing,” *Appl. Sci.* **9**, 1609 (2019).
- [66] Xianli Su, Na Zhao, Shiqiang Hao, Constantinos C Stoumpos, Mengyuan Liu, Haijie Chen, Hongyao Xie, Qingjie Zhang, Chris Wolverton, Xinfeng Tang, *et al.*, “High thermoelectric performance in the wide band-gap $\text{AgGa}_{1-x}\text{Te}_2$ compounds: Directional negative thermal expansion and intrinsically low thermal conductivity,” *Adv. Funct. Mater.* **29**, 1806534 (2019).
- [67] Panida Pilasuta, Pennapa Muthitamongkol, Chanchana Thanachayanont, and Tosawat Seetawan, “Characterization of $\text{Zn}_{0.96}\text{Al}_{0.02}\text{Ga}_{0.02}\text{O}$ Thermoelectric Material,” *Adv. Mater. Res.* **802**, 227–231 (2013).